FULL PAPER

Scaling Behavior of Resistive Switching in Epitaxial Bismuth Ferrite Heterostructures

Abhimanyu Rana, Haidong Lu, Kashinath Bogle, Qi Zhang, Rama Vasudevan, Vishal Thakare, Alexei Gruverman, Satishchandra Ogale,* and Nagarajan Valanoor**

Resistive switching (RS) of (001) epitaxial multiferroic $BiFeO_3$/$La_{0.67}Sr_{0.33}MnO_3$/$SrTiO_3$ heterostructures is investigated for varying lengths scales in both the thickness and lateral directions. Macroscale current–voltage analyses in conjunction with local conduction atomic force microscopy (CAFM) reveal that whilst both the local and global resistive states are strongly driven by polarization direction, the type of conduction mechanism is different for each distinct thickness regime. Electrode-area dependent studies confirm the RS is dominated by an interface mechanism and not by filamentary formation. Furthermore, CAFM maps allow deconvolution of the roles played by domains and domain walls during the RS process. It is shown that the net polarization direction, and not domain walls, controls the conduction process. An interface mechanism based on barrier height and width alteration due to polarization reversal is proposed, and the role of electronic reconstruction at the interface is further investigated.

1. Introduction

Resistive switching (RS) in epitaxial ferroelectric heterostructures has attracted immense interest due to its potential use in nanoelectronic devices.[1] A particular case of RS-based ferroelectric devices is the so-called ferroelectric tunnel junction [4,5] wherein manipulation of the local polarization leads to the tunneling electroresistance (TER) effect.[6] Often termed as "polarization mediated electron transport", TER has been extended to demonstrate multiferroic tunneling barriers,[7–9] interface-induced exchange bias (EB),[10] ferroelectric control of magnetotransport[5,11] and ferroelectric memristors.[12] In addition to TER, mechanisms such as nucleation and growth of ferroelectric domains,[12] filamentary conduction,[13] and scanning probe tip-induced effects[14,15] have also been shown to cause RS in ferroelectrics.

It is known that in complex oxide heterostructures the dominant functional or structural parameter is often spatially inhomogeneous.[16] This is particularly important in complex oxides where multiple physical interactions (e.g., spin, polarization charge, lattice, and/or octahedral tilts) can coexist. Given the intimate lattice-polarization coupling in ferroelectric thin films, naturally occurring spatial inhomogeneities, such as domains and domain walls, are expected to play a critical role in the RS of ferroelectric devices. This is particularly relevant given the recent finding that certain types of domain walls in bismuth ferrite can conduct whilst the domains themselves remain insulating.[17] This has led to the idea that the transport properties of the system may be determined by the walls as opposed to the domains.[18] Following the finding of Seidel et al.,[17] domain wall conduction has been shown to be present in a wider range of ferroelectrics, from $PbZr_{0.2}Ti_{0.8}O_3$ (PZT),[19] to hexagonal manganites[17] and even $LiNbO_3$.[20] Concurrently, an idea that has gained acceptance is that the electrical boundary conditions in ultrathin epitaxial ferroelectrics (created due to the band offsets at the interfaces) can result in one polar state, that is, one polar domain, being intrinsically more conductive than the other.[4,5] On the other hand it has been shown that one has to also be aware of filamentary mechanisms which necessitate concurrent measurement of both polarization switching (for example using strain or capacitance–voltage butterfly loops) and resisitive switching to see if the voltage threshholds for both processes coincide.[21]

In this study, we exploit the thickness of the ferroelectric layer as a powerful control parameter to gain a deeper understanding of the mechanisms that control RS in bismuth ferrite thin film heterostructures. It is well-known that domain wall

Dr. A. Rana,[+] Dr. K. Bogle,[++] Q. Zhang, Dr. R. Vasudevan,[+++] Prof. N. Valanoor
School of Materials Science and Engineering
University of New South Wales (UNSW)
Sydney 2052, Australia
E-mail: nagarajan@unsw.edu.au
Dr. A. Rana, V. Thakare, Prof. S. Ogale
Physical and Materials Chemistry Division
NCL, CSIR, Pune 411008, India
E-mail: sb.ogale@ncl.res.in
Dr H. Lu, Prof. A. Gruverman
Department of Physics & Astronomy
University of Nebraska
Lincoln NE 68588-0111, USA
E-mail: Alexei_Gruverman@unl.edu
[+]Present address: NUSNNI-NanoCore, National University of Singapore, Singapore, 117411
[++]Present address: School of Physical Sciences, Swami Ramanand Teerth Marathawada University, Nanded, 431606, India
[+++]Present address: Center for Nanophase Materials Sciences, Oak Ridge National Laboratory, Oak Ridge TN 37831 USA

DOI: 10.1002/adfm.201400110

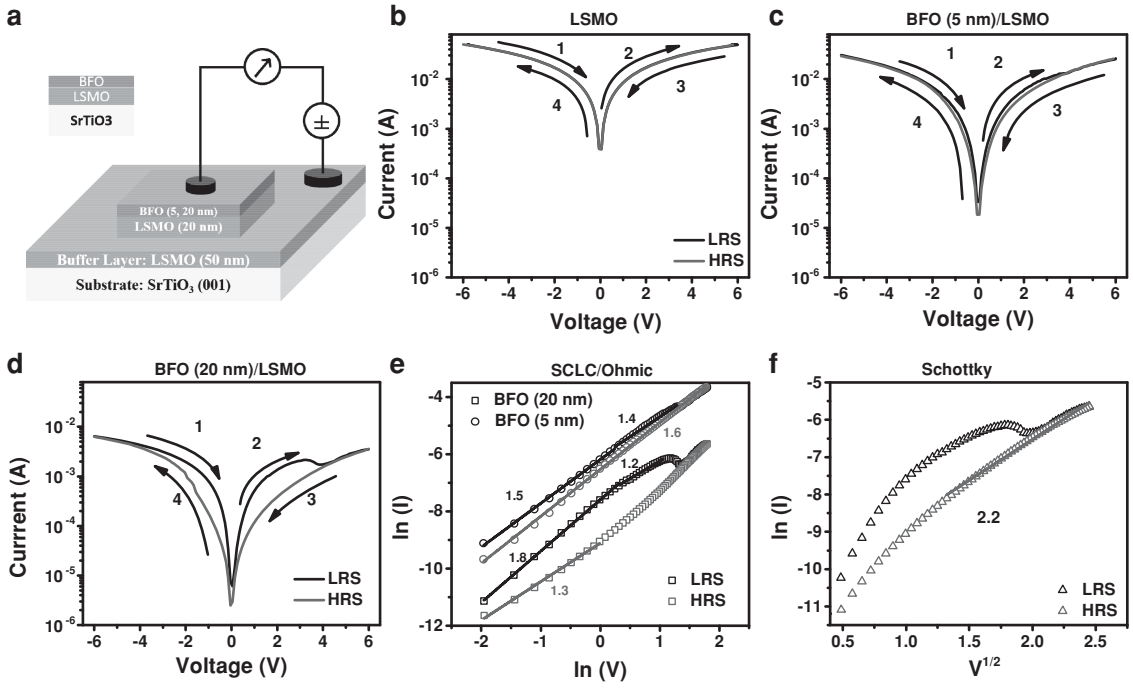

Figure 1. a) Schematic showing the device architecture in current perpendicular to plane (CPP) configuration. Current-voltage (*I–V*) acquired using 200 μm × 200 μm Pt pads for b) bare $La_{0.67}Sr_{0.33}MnO_3$ (LSMO) thin film, c) 5 nm $BiFeO_3$ (BFO) on LSMO, and d) 20 nm BFO on LSMO. e) Linear fitting using space charge limited conduction (SCLC)/Ohmic equations for the 5 nm and 20 nm cases. Note the SCLC/Ohmic fits work for both, the low resistive state (LRS) and the high resistive state (HRS) states of 5 nm film but only the LRS state for the 20 nm film. f) Linear fitting by Schottky emission of the HRS state of the 20 nm film.

morphology, in terms of their shape and periodicity, is strongly driven by the thickness of the ferroelectric.[18,22] Here we demonstrate that the film thickness is not only an effective parameter to tune the ferroelectric domain wall morphology[18,22] but can also be exploited to modulate the magnitude and type of polarization-mediated RS in ferroelectric heterostructures.

Epitaxial (001) $(BiFeO_3)/(La_{0.67}Sr_{0.33}MnO_3)$ (BFO/LSMO) structures are chosen as the model materials systems where the thickness of the sandwiched ferroelectric layer is either 5 nm or 20 nm. We restrict the thickness of BFO to such dimensions since significantly different volume fractions of these films are under depletion or accumulation conditions as a result of band-bending at the top and bottom interfaces, which allows us to evaluate the role of this effect in RS behavior.[23] Macroscale current-voltage (*I–V*) measurements as a function of electrode area, in conjunction with local scanning probe microscopy (SPM)-based measurements find that both the local and global resistive states are strongly dependent on the polarization orientation of BFO layer. Whilst polarization control of conduction in ferroelectrics has been shown before,[2,4,8,9,12,15] we show here that the fundamental mechanism that controls the resistive states is different for each BFO film thickness. Whilst RS is governed by tunneling for the thinner 5 nm BFO thickness, for the thicker 20 nm films it is controlled by Schottky emission. Furthermore, whilst it is impossible to completely rule out filamentary formation or oxygen vacancy migration, electrode area-dependent measurements hint that these are not the dominant RS mechanism. Based on these experimental results, we propose a mechanism based on barrier height and width alteration due to polarization reversal, and further elaborate on the role of electronic reconstruction at the interface to explain the obtained results.

2. Results and Discussion

(001) oriented BFO/LSMO heterostructures were grown on vicinally miscut (001) $SrTiO_3$ substrates by pulsed laser deposition (PLD) under reflection high-energy electron diffraction (RHEED) monitoring to ensure atomically sharp interfaces in the thin films.[9,24] **Figure 1**a shows the schematic of the measured device architecture (see Experimental Section for fabrication details) having platinum pads (200 μm × 200 μm) as top contacts. Here, the current perpendicular to plane (CPP) configuration (which is a distinct change from previous studies) was employed to measure the electron transport across the heterostructures. The CPP architecture was employed as it is a well-known technique to avoid complexities that arise from an additional (imperfect) interface between the bottom oxide electrode (LSMO) and the substrate.[25] Macroscale *I–V* curves were recorded by sweeping a triangular ramp from negative to positive bias (forward branch) and then back (reverse branch). Repeated datasets are provided in Supporting Information S1 that confirm reproducibility. The polarity of electric field refers to the voltage applied to the top contact. Figure 1b–d show the *I–V* characteristics of the bare LSMO thin films, BFO(5 nm)/LSMO(20 nm) and BFO(20 nm)/LSMO(20 nm) films, respectively, obtained in CPP geometry. No switching hysteresis is

observed for the bare LSMO thin films Figure 1b, which indicates any measured hysteresis for the other cases does not stem from the bottom LSMO/LSMO interface. Figures 1c,d show the clear opening of hysteresis and particularly in the case of the 20 nm film a large broadening of loop with a shift in the current at zero bias, which confirms RS behavior. The black curve is the original low resistive state (LRS) and red curve is the final high resistive state (HRS). Datasets acquired from various other pads are shown in Supporting Information S1. Therefore, the observed phenomenon could be attributed to features specific to the multiferroic/electrode interface, namely BFO/LSMO, investigated here.

To investigate the detailed nature of RS, we fitted these results to various possible transport mechanisms, such as, direct electron tunneling, Fowler-Nordheim (FN) tunneling, space charge limited conduction (SCLC), Schottky emission and Poole-Frenkel (PF) emission assuming a simple metal-insulator-metal/semiconductor type structure. The value of the static dielectric constant extracted from the fits (≈23) was used for validation purpose (full discussion of the fitting and the dielectric constants is given in the Supporting Information S2).[26] Capacitance measurement of these pads revealed a saturation dielectric constant of 25 @ 100 KHz (not shown here) and therefore lend credence to the extracted value. The Ohmic and SCLC mechanisms should follow a linear relation between ln (I) versus ln (V) with slopes ≈1 and ≈2, respectively. On the other hand, the Schottky and PF mechanisms can be fitted by the Equations 1,2, respectively

$$\ln(I) = \frac{\sqrt{e^3 / 4\pi\varepsilon_0\varepsilon_r d}}{kT} V^{1/2} \tag{1}$$

$$\ln(I/V) = \frac{\sqrt{e^3 / \pi\varepsilon_0\varepsilon_r}}{rkT} V^{1/2} \tag{2}$$

where e is electronic charge, k the Boltzmann constant, ε_0 is permittivity of free space, ε_r is the dielectric constant, r is a constant that varies from 1 to 2 depending of position of the Fermi level. The difference between these mechanisms is that the Schottky and PF are interface and bulk limited emissions, respectively.

The other possible conduction mechanism is electron tunneling, which can be well described by Simmons's expression as given below

$$I = \frac{eA}{4\pi^2\hbar d^2}\left\{\left(\phi - \frac{eV}{2}\right)\exp\left(-\frac{2d\sqrt{2m_e}}{\hbar}\sqrt{\phi - \frac{eV}{2}}\right) - \left(\phi + \frac{eV}{2}\right)\exp\left(-\frac{2d\sqrt{2m_e}}{\hbar}\sqrt{\phi + \frac{eV}{2}}\right)\right\} \tag{3}$$

where e is electronic charge, ϕ the barrier height, A is contact area, d the barrier width which is the thickness of film, m_e is electron effective mass.

For different voltage regimes the Simmons equation can be simplified by assuming a rectangular barrier near zero bias voltages (direct tunneling) and triangular barriers at much higher voltages when eV >> ϕ (FN tunneling) as given by the Equations 4,5, respectively.

$$I \propto V \exp\left(-\frac{2d\sqrt{2m_e\phi}}{\hbar}\right) \tag{4}$$

$$I \propto V^2 \exp\left(-\frac{2d\sqrt{4m_e\phi^3}}{3eV\hbar}\right) \tag{5}$$

The fitting results are shown in Figures 1e,f. For the 5-nm-thick BFO films, both the LRS and the HRS states can be fitted by Ohmic/SCLC (due to direct tunneling or trap assisted tunneling) as shown in Figure 1e. On the other hand, for 20-nm-thick BFO films only the LRS could be fitted with SCLC [Figure 1(e)] whilst the HRS can be fitted by Schottky emission (Figure 1f). The slope values of linear fits are indicated on the respective plots.

The fits (see also Supporting Information Figure S2) indicate that for the 5-nm-thick BFO films electron tunneling is the dominant conduction mechanism for RS and the origin of RS is adequately described by the modulation of tunneling barrier by polarization switching in the ferroelectric layer.[2,4,8,9,15] However, in the thicker BFO films (20 nm) the RS stems from an interface-limited Schottky emission through the conduction band of BFO and not from tunneling. Previously reported work[26] on significantly thicker epitaxial (001) BFO films (≈175 nm) with bottom $SrRuO_3$ electrodes (≈50 nm) on $DyScO_3$ substrate attributed the origin of leakage current in BFO to bulk-limited PF emission due to oxygen vacancies. Importantly, no SCLC was found. In the present case, both thicknesses show strong RS hysteresis with a large suppression of bulk-limited leakage current. The fitting of LRS by Ohmic or SCLC and HRS by Schottky emission is a well-known signature of an interface-based mechanism[3,27] thus suggesting that the RS is controlled by the direction of the polarization. However, it is also necessary to check if the observed RS has (dominant) contributions from any filamentary processes.

Figure 2a shows I–V characteristics acquired using top electrodes of different area for both films. Investigating the area-dependence of RS is an effective method to distinguish between filamentary and interfacial conduction. In filamentary type conduction, the resistance is independent of top electrode area.[27] On the other hand, in case of interfacial RS there are no variations in local resistivity (ρ) over the measured area (A) and hence the resistance should linearly decrease with area ($R \approx \rho\, d\, /A$) for constant film thickness (d). To check for this effect, I–V characteristics for three different circular electrodes of radius (r) ≈ 50, 100, and 200 μm were acquired. Additionally I–V loops were acquired using the conductive atomic force microscopy (CAFM) tip as an extreme case of nanoscale electrode area. Indeed, a reduction in the magnitudes of current for larger electrodes was observed (Figure 2). Figure 2b shows resistance, approximated by fitting the linear range of I–V characteristics as a function of the electrode area for three circular electrodes and the CAFM tip. Resistance significantly increases with decreasing electrode area thus confirming the dominating role of the interfacial type of conduction mechanism. We must reiterate that it is not possible to fully rule out filamentary or oxygen vacancies mechanisms in any transport measurements of oxide heterostructures. These mechanisms stem from defects created during film growth, which are typically under

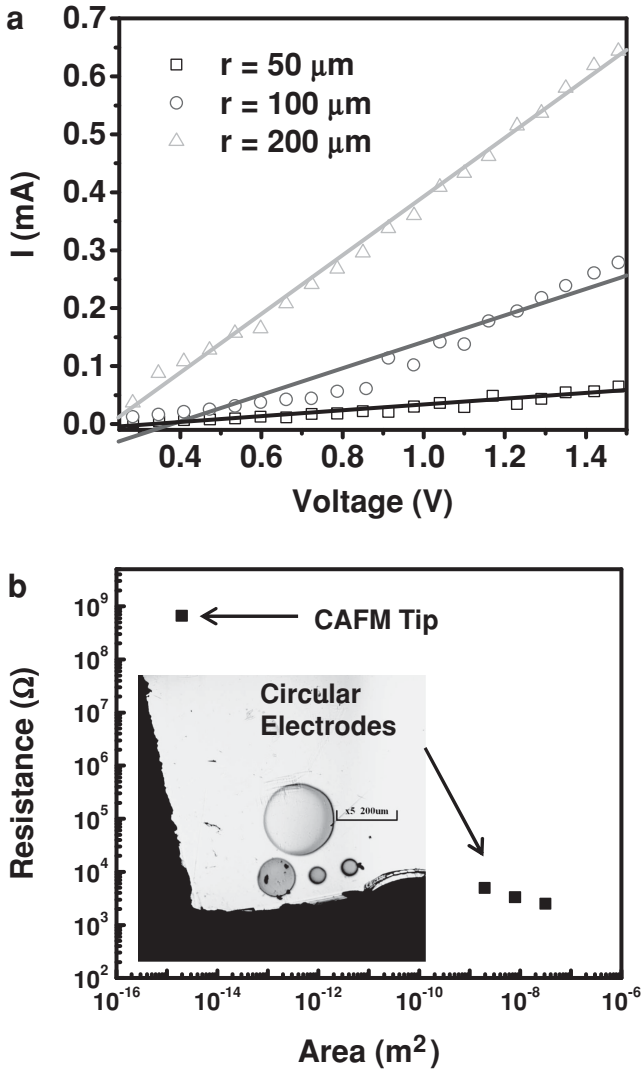

Figure 2. a) Linear part of the I-V plots acquired for three different circular electrode sizes. (50, 100, and 200 μm diameter respectively). b) Resistance of the junction as a function of electrode size (three circular electrodes and the atomic force microscope tip). The inset shows the images of circular electrodes used.

conditions of high temperatures and vacuum. AFM tip-induced oxygen vacancy effects can be quite strong in oxide thin films. Nevertheless, since we measure the RS using large top electrodes, the results discussed above indicate that were such filamentary or oxygen vacancy mechanisms present, they would not dominate the RS mechanism.

We now turn to understanding the role of the local polarization state in controlling the RS for each thickness. A number of models, based on spatial inhomogeneities or variations in band structure have been proposed for RS in complex perovskite oxides[28,29] Thus, in order to understand the role of spatial variations in the polarization it is first necessary to characterize the nature and morphology of the ferroelectric domains in the BFO layers. For this purpose, dual amplitude resonance tracking piezoresponse force microscopy (DART-PFM) measurements were carried out. **Figure 3** shows 500 nm × 500 nm out-of-plane PFM amplitude, PFM phase and CAFM maps acquired in the 5-nm-thick and 20-nm-thick films, respectively. Larger 1 μm × 1 μm PFM scans are shown in Supporting Information Figure S3. The amplitude and phase images reveal that the films are in a poly-domain state with distinct fractal-like domain walls. Such fractal-like domains are observed typically for very thin BFO films.[22] The walls do not adhere to any strict crystallographic directions and hence cannot be considered as ferroelastic.[30,31] These are 180° domain walls that have been previously found to be conductive.[17] The images reveal a higher domain density for the thinner films and the average domain size, evaluated using the autocorrelation analysis (see Supporting Information Figure S4), increases with the film thickness. The reduction of domain size with film thickness can be understood from Kittel relationship ($w \propto \sqrt{t}$).[32] Detailed theoretical understanding of the ferroelectric domain structures and size with film thickness has been previously presented by Catalan et al.[18]

In conjunction with PFM images, the CAFM current maps reveal two vital pieces of information. Firstly, they show spatially inhomogeneous current regions that directly correlate with a particular direction of the polarization. Irrespective of thickness, the polarization direction pointing downwards bears a direct correspondence with the LRS. This reinforces conclusions from Figure 2 that the dominant conduction mechanism is controlled by the polarization state and not the presence of filaments. Secondly, we find that the local variations in the polarization magnitude (not just the direction) strongly affect the current. In other words, there is a strong signature of polarization-magnitude mediated current transport in our films.

It is worth noting that the information revealed by the CAFM images in Figure 3 is different from prior key findings in BFO,[17,30,33] which maintain that the domains typically have conductivity lower than the domain walls. Similarly, in the case of PZT thin films, it has been shown that domain walls possess greater conductivity than the domains.[19] On the other hand, domain wall conductivity was found to be sensitive to annealing, which suggests that this characteristics is not a universal property of the domain walls, but depends on specific conditions, such as film processing parameters.[19,30,33] Hence, it is critical to delineate domain wall contribution from the domains to the conduction current. Unfortunately, Figures 3c,f do not have the resolution to confidently separate domain wall conduction from the domain contribution. Therefore, an alternative approach based on PFM hysteresis loop analysis was employed in order to understand the role played by the domain walls vis-à-vis the domains.

In **Figure 4** we plot the PFM switching loops acquired both, locally on a single point (Figure 4a, 5 nm, and Figure 4b, 20 nm) and on 50 μm × 50 μm pads (Figure 4c, 5 nm, and Figure 4d, 20 nm) respectively. (Statistical samples provided in S5,S6) There is a certain degree of imprint in the local measurements attributed to the asymmetrical electrical boundary conditions. A sharp 180° change in the PFM phase coupled with the dip in the PFM amplitude occurs at ± 0.9 V for the 5 nm and at ± 2 V for the 20 nm BFO films which indicate local coercive voltages for these films. In contrast, the coercive voltages obtained from the corresponding loops acquired on top electrode pads equate to ± 3 and ± 4 for 5 nm and 20 nm films, respectively. At these values a corresponding sharp transition

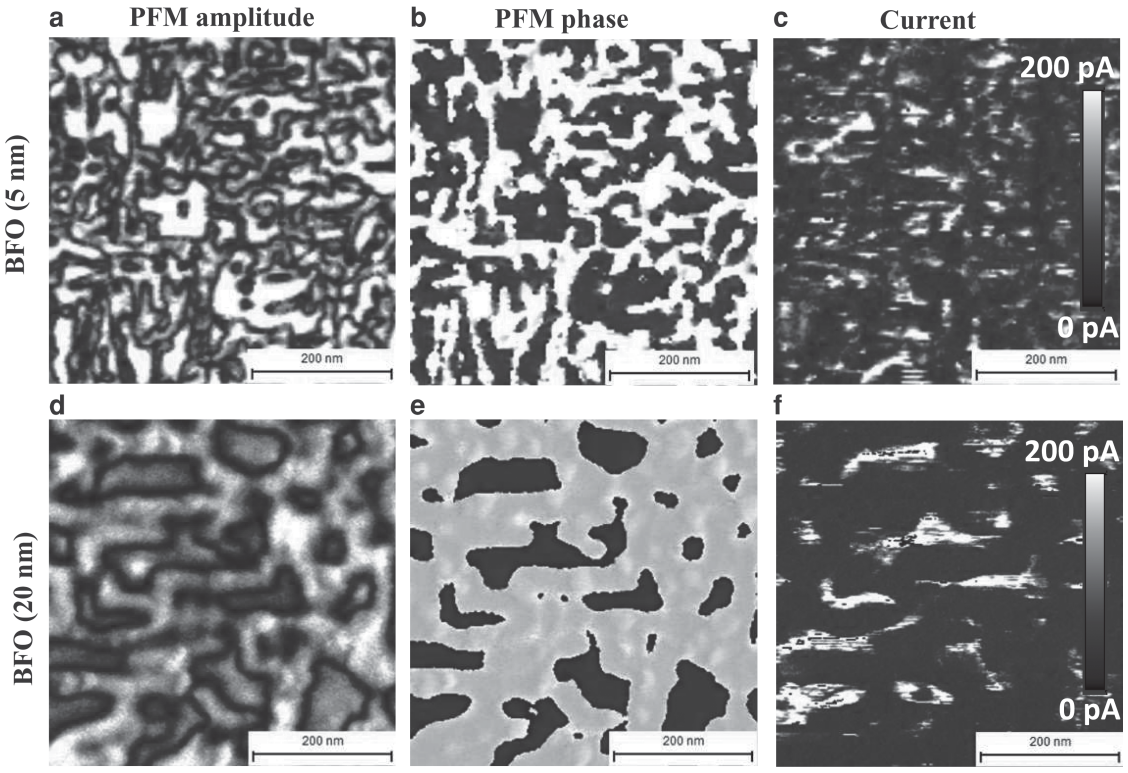

Figure 3. Dual amplitude resonance tracking-piezoresponse force microscopy (DART-PFM) images of a,d) amplitude and b,e) phase, and c,f) conduction atomic force microscopy (C-AFM) current images for a–c) the 5 nm and d–f) the 20 nm $BiFeO_3$ films.

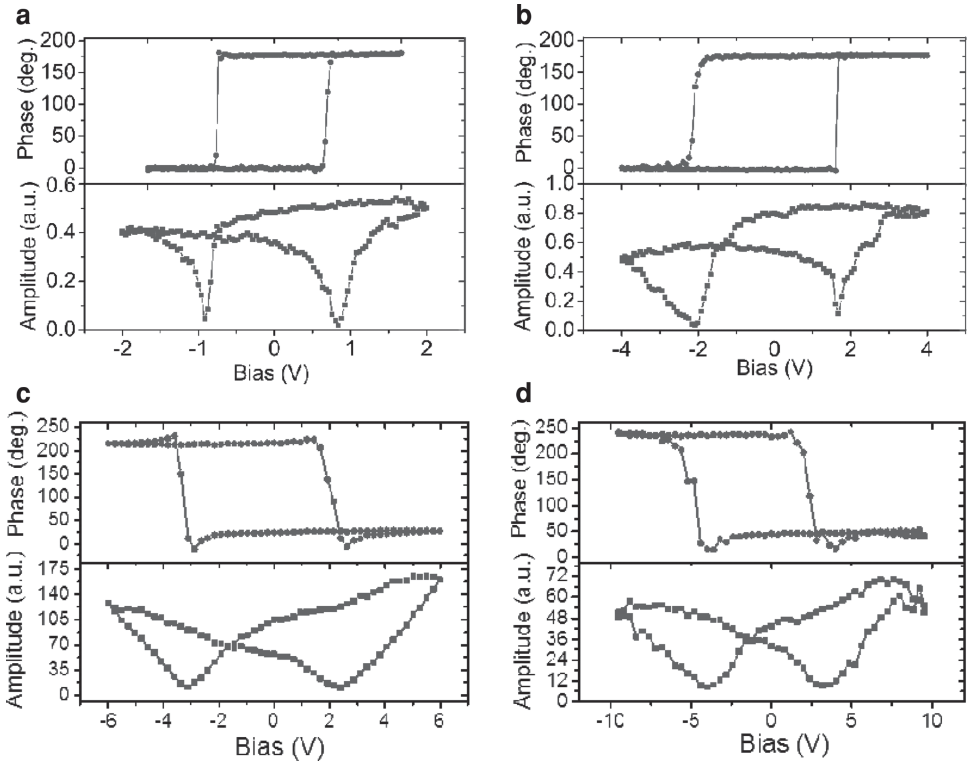

Figure 4. Single point PFM hysteresis (phase and amplitude) for the a) 5 nm and b) 20 nm films c) with pad on 5 nm film and d) with pad on 20 nm film.

between the LRS to HRS states is observed in the macroscale *I–V* measurements. We have also acquired DC strain loops (Supporting Information Figure S3) that further corroborate the alignment of the coercive voltage values with the observed jump in the *I–V* measurements from Figure 1. Following the discussion given by Kohlstedt et al[21] this indicates that the observed *I–V* hysteresis in Figure 1 stems from the polarization switching. We sought further visual evidence to check how the switching of all domains in one direction alters the global resistive state.

CAFM scans were acquired after performing DC bias writing on the same films. Generation of downward oriented domains was first achieved by scanning an area of 1 μm × 0.5 μm under external DC bias of + 3 V applied to the tip. This was followed by poling to the upward state by scanning under external DC bias of –3 V in the adjacent 1 μm × 0.5 μm area. The subsequent current map acquired at 0.8 V for the 5-nm-thick film as shown in **Figure 5**a (see Supporting Information Figure S6 for data on the 20-nm-thick film) illustrates a direct correlation of the low and high resistance states with the down and up domain orientations, which is consistent with data obtained for the as-grown BFO films (Figure 3). The spatial inhomogeneity of current is also significantly reduced in the poled regions as the volume fraction of switched domains is much higher. Figure 5b compares three *I–V* curves acquired for as grown upward- and downward-oriented domains and at the domain wall using the CAFM tip. The inset to the Figure 5b is the high-resolution PFM image, which shows the locations at which the data were acquired. Figure 5b confirms that the walls are less conducting than the domains, and that the two domain states do act as two back-to-back Schottky diodes as noted previously.[3,19] They also confirm the highly asymmetric diode-like characteristics with forward to reverse bias current ratio of ~10^3 as observed by others.[3,34] We also investigated the *I–V* characteristics of the poled regions for both film thicknesses, (Figure 5c). Most importantly, Figure 5b,c illustrates that the voltage, at which onset of large increase in conduction is observed, aligns well with the coercive voltages acquired from the local single point measurements (Figure 4a,b) for each film thickness. This confirms that the change in resistance is indeed driven by polarization switching. Figure 5d shows the linear fitting of these curves by FN tunneling, which occurs due to the significant reduction of the barrier width at higher fields. However, in this case the FN tunneling occurs through the modified Schottky barrier due to the localized nature of the electric field under a tip.[15] Importantly, the Schottky barrier height approximated from these curves is increased from ≈0.25 V to ≈0.5 V with increase in the BFO film thicknesses from 5 nm to 20 nm, as shown by the arrow mark in Figure 5d. We also note the highly asymmetric nature of *I–V* curves, which is absent

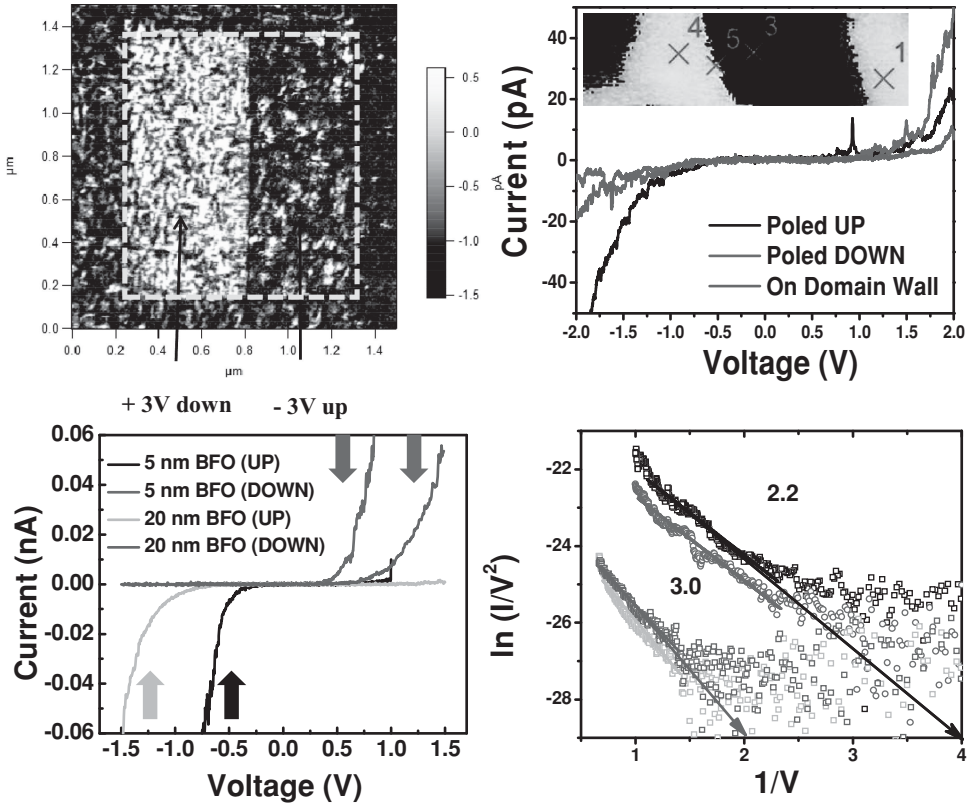

Figure 5. a) C-AFM map acquired at 0.8 V for the 5 nm $BiFeO_3$ film after ±3 V bias. Regions of the film that are poled downward (+3 V) display a higher current compared to regions that are poled upward (–3 V). b) Current–voltage (*I–V*) curves for the as-grown up, as-grown down and at the domain wall for the 5 nm film. The inset is a high-resolution DART-PFM image showing where the *I–V* curves were acquired. c) *I–V* curves acquired for the poled regions of Figure 5a and Supporting Information Figure S4. d) Fitting of curve (c) by Fowler-Nordheim tunneling current.

in the corresponding macroscale measurements (Figure 1), highlighting the role of local tip potential effects on the Schottky barrier.[14,15]

We do note that we did not observe any sign of cycle-to-cycle non-reproducibility in the switching behavior in these films. There are spatial, point-to-point variations in the local conductivity within large-scale (several square micrometers) single domains (Supporting Information Figure S6). These variations could be due to a) the surface topographic features, which affect the tip-sample contact resistance, b) remanent domains left after poling or local polarization switching induced during C-AFM imaging, and c) local variations in polarization magnitude due to defect structure as observed from the local hysteresis loops. However, these variations in general are smaller in magnitude than the difference in conductivity between the opposite domains.

Figure 6 illustrates the possible RS mechanism governed by electric polarization. The electronic charge inside the manganite layer can be screened by changing the electron/hole charge density (that can also lead to an interfacial metal-insulator transition[29,35] in response to the polarization within the BFO layer. Therefore, the polarization direction inside the BFO layer can modulate the charge density at the interface leading to Schottky type bend bending (underlying the need for ultra-thin films) and hence hysteresis. During forward bias (positive voltage to LSMO) in Figure 6a, a polarization is gradually developed inside BFO. The developed polarization inside BFO can increase the barrier height[8] thus causing the depletion of electronic charge at the interface leading to band bending. After a critical voltage is achieved the polarization built inside BFO leads to sufficient increase in barrier height and width to suppress the SCLC (due to tunneling and transport through impurity states). The system after this point is switched into HRS and follows Schottky emission. Even though the system is returned back to original zero bias condition as shown in Figure 6b, the altered band structure (responsible for HRS) remains due to remnant polarization inside BFO. The *I–V* characteristic follows the HRS via Schottky emission until the reverse polarization switching occurs where the system is returned to its original LRS.

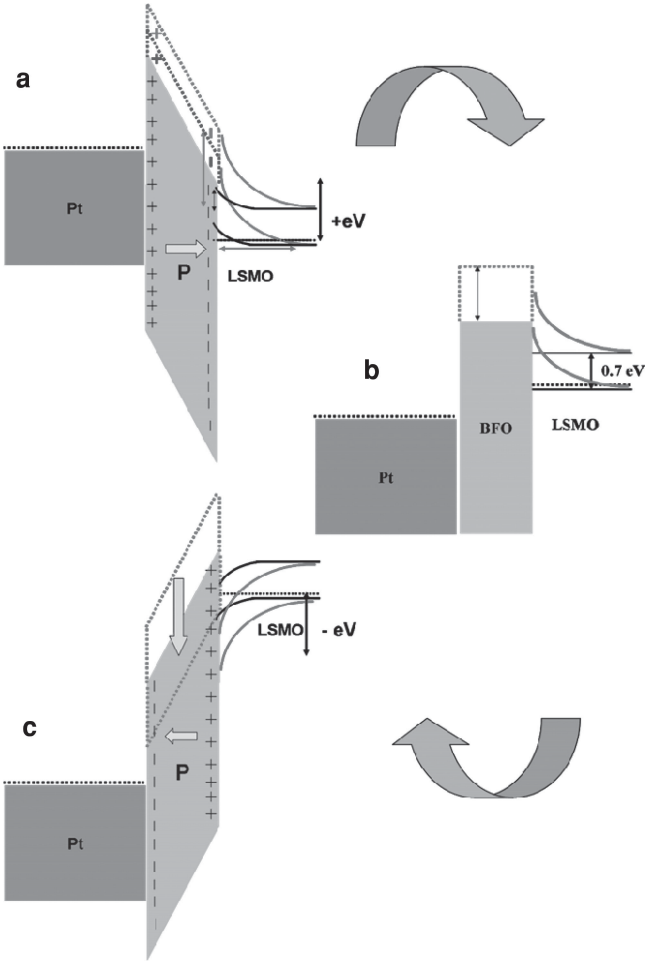

Figure 6. Schematic diagram for proposed mechanism for polarization induced Schottky barrier modification for resistive switching: Band diagram during a) forward bias, b) intermediate zero bias, and c) reverse bias.

3. Conclusion

In summary, we investigate the resistive switching behavior of epitaxial (001) BFO/LSMO heterostructures by combining local SPM with macroscale measurements for two distinct thickness regimes. It is found that the local variations in the domain structure lead to spatially inhomogeneous current. The local resistive state is controlled by polarization orientation of a ferroelectric domain. Specifically, the downward-oriented domains are found to be more conductive compared to the upward domains. In contrast, domain walls were found to be less conductive than the domains of either polarity and hence the domains (as opposed to domain walls) dominate the transport behavior for these ultra-thin epitaxial heterostructures. X-ray magnetic circular dichroism studies have already revealed that the orbital reconstruction at the interface leads to superexchange coupling across the BFO/LSMO interface causing novel magnetic states and EB effects.[10] The results reported here lead to further questions on the temperature and magnetic field effects on resistive switching and open new avenues to exploit correlations between transport, magnetic and ferroelectric properties in CPP configuration devices such as for example, polarization control of electronic states in strongly correlated oxide heterostructures.[36]

4. Experimental Section

The device architecture (as shown in Figure 1a) is fabricated by PLD using a KrF excimer laser (λ = 248 nm, 20 ns pulse duration) under RHEED control. Full details are given elsewhere.[9] The substrate was annealed in vacuum at 900 °C for 30 min prior to deposition. Initially, a 50 nm LSMO buffer layer was deposited on single crystal (001) $SrTiO_3$ substrate (with 0.1° vicinal miscut along (010) – Shinkosa Japan) at 900 °C temperature, laser density ≈1.3 J cm^{-2}, laser frequency 5 Hz and oxygen pressure 100 mTorr. The sample was cooled at oxygen pressures 600 Torr at cooling rate 5 °C min^{-1}. Vacuum was then broken and an edge of the wafer masked off such that masked portion of the LSMO layer serves as the bottom electrode in a CPP configuration. A 20 nm

thick LSMO bottom layer was deposited again followed by a thin BFO (5 nm or 20 nm) top layer. The BFO was deposited at 850 °C, laser density ≈0.9 J cm^{-2}, laser frequency 10 Hz and oxygen pressure 50 mTorr. The sample was cooled in oxygen at 400 Torr at 20 °C min^{-1} cooling rate. The epitaxial quality was confirmed by θ–2θ and reciprocal space mapping X-ray diffraction analysis. X-ray reflectometry (XRR) was used to ascertain film thickness (Supporting Information S7). High-resolution transmission electron microscopy on similar set of samples has shown the interfaces are sharp without secondary phases or stacking faults etc.[9] PFM and CAFM measurements were carried out concurrently on the same machine (Asylum MFP-3D). Macroscale I-V characteristics were measured as a function of different electrode sizes using a Keithley 2400 current–voltage source meter instrument. For PUND, PFM loops and DC strain loops, 23 μm × 23 μm Au/Ti (60 nm/5 nm in thickness) pads were defined on the sample surface as the top electrode through photolithography and metal evaporation.

Acknowledgements

A.R. and H.L. contributed equally to this work. This work is supported by an Australia India Strategic Research Fund ST020078. The authors at NCL acknowledge the grant from DST and CSIR network project NWP051. R.V. and V.N. acknowledge the support of an ARC Discovery Grant and LIEF equipment grant. H.L. and A.G. acknowledge support of Nebraska Research Initiative and Nanoelectronics Research Initiative (NRI) Center for NanoFerroic Devices (CNFD).

Received: January 13, 2014
Published online: March 18, 2014

[1] a) V. Garcia, M. Bibes, L. Bocher, S. Valencia, F. Kronast, A. Crassous, X. Moya, S. Enouz-Vedrenne, A. Gloter, D. Imhoff, C. Deranlot, N. D. Mathur, S. Fusil, K. Bouzehouane, A. Barthelemy, *Science* **2010**, *327*, 1106; b) M. H. Park, H. J. Lee, G. H. Kim, Y. J. Kim, J. H. Kim, J. H. Lee, C. S. Hwang, *Adv. Funct. Mater.* **2011**, *21*, 4305; c) R. Waser, R. Dittmann, G. Staikov, K. Szot, *Adv. Mater.* **2009**, *21*, 2632.

[2] A. Gruverman, D. Wu, H. Lu, Y. Wang, H. W. Jang, C. M. Folkman, M. Y. Zhuravlev, D. Felker, M. Rzchowski, C. B. Eom, E. Y. Tsymbal, *Nano Lett.* **2009**, *9*, 3539.

[3] A. Q. Jiang, C. Wang, K. J. Jin, X. B. Liu, J. F. Scott, C. S. Hwang, T. A. Tang, H. Bin Lu, G. Z. Yang, *Adv. Mater.* **2011**, *23*, 1277.

[4] a) E. Y. Tsymbal, H. Kohlstedt, *Science* **2006**, *313*, 181; b) C. G. Duan, R. F. Sabirianov, W. N. Mei, S. S. Jaswal, E. Y. Tsymbal, *Nano Lett.* **2006**, *6*, 483.

[5] Y. W. Yin, J. D. Burton, Y. M. Kim, A. Y. Borisevich, S. J. Pennycook, S. M. Yang, T. W. Noh, A. Gruverman, X. G. Li, E. Y. Tsymbal, Q. Li, *Nat. Mater.* **2013**, *12*, 397.

[6] C.-G. Duan, S. S. Jaswal, E. Y. Tsymbal, *Phys. Rev. Lett.* **2006**, *97*, 047201.

[7] A. Chanthbouala, A. Crassous, V. Garcia, K. Bouzehouane, S. Fusil, X. Moya, J. Allibe, B. Dlubak, J. Grollier, S. Xavier, C. Deranlot, A. Moshar, R. Proksch, N. D. Mathur, M. Bibes, A. Barthelemy, *Nat. Nanotechnol.* **2012**, *7*, 101.

[8] M. Gajek, M. Bibes, S. Fusil, K. Bouzehouane, J. Fontcuberta, A. Barthelemy, A. Fert, *Nat. Mater.* **2007**, *6*, 296.

[9] M. Hambe, A. Petraru, N. A. Pertsev, P. Munroe, V. Nagarajan, H. Kohlstedt, *Adv. Funct. Mater.* **2010**, *20*, 2436.

[10] S. M. Wu, S. A. Cybart, P. Yu, M. D. Rossell, J. X. Zhang, R. Ramesh, R. C. Dynes, *Nat. Mater.* **2010**, *9*, 756.

[11] a) D. Pantel, S. Goetze, D. Hesse, M. Alexe, *Nat. Mater.* **2012**, *11*, 289; b) J. D. Burton, E. Y. Tsymbal, *Phys. Rev. Lett.* **2011**, *106*, 157203.

[12] A. Chanthbouala, V. Garcia, R. O. Cherifi, K. Bouzehouane, S. Fusil, X. Moya, S. Xavier, H. Yamada, C. Deranlot, N. D. Mathur, M. Bibes, A. Barthelemy, J. Grollier, *Nat. Mater.* **2012**, *11*, 860.

[13] a) K. Szot, W. Speier, G. Bihlmayer, R. Waser, *Nat. Mater.* **2006**, *5*, 312; b) A. Sawa, *Mater. Today* **2008**, *11*, 28.

[14] M. Alexe, D. Hesse, *Nat. Commun.* **2011**, *2*, 1.

[15] P. Maksymovych, S. Jesse, P. Yu, R. Ramesh, A. P. Baddorf, S. V. Kalinin, *Science* **2009**, *324*, 1421.

[16] E. Dagotto, *Science* **2005**, *309*, 257.

[17] J. Seidel, L. W. Martin, Q. He, Q. Zhan, Y. H. Chu, A. Rother, M. E. Hawkridge, P. Maksymovych, P. Yu, M. Gajek, N. Balke, S. V. Kalinin, S. Gemming, F. Wang, G. Catalan, J. F. Scott, N. A. Spaldin, J. Orenstein, R. Ramesh, *Nat. Mater.* **2009**, *8*, 229.

[18] G. Catalan, J. Seidel, R. Ramesh, J. F. Scott, *Rev. Mod. Phys.* **2012**, *84*, 119.

[19] J. Guyonnet, I. Gaponenko, S. Gariglio, P. Paruch, *Adv. Mater.* **2011**, *23*, 5377.

[20] M. Schroder, A. Haussmann, A. Thiessen, E. Soergel, T. Woike, L. M. Eng, *Adv. Funct. Mater.* **2012**, *22*, 3936.

[21] H. Kohlstedt, A. Petraru, K. Szot, A. Rudiger, P. Meuffels, H. Haselier, R. Waser, V. Nagarajan, *Appl. Phys. Lett.* **2008**, *92*, 062907.

[22] G. Catalan, H. Béa, S. Fusil, M. Bibes, P. Paruch, A. Barthélémy, J. F. Scott, *Phys. Rev. Lett.* **2008**, *100*, 027602.

[23] a) J. Chen, H. Lu, H. J. Liu, Y. H. Chu, S. Dunn, K. Ostrikov, A. Gruverman, N. Valanoor, *Appl. Phys. Lett.* **2013**, *102*, 182904; b) S. Dunn, P. M. Jones, D. E. Gallardo, *J. Am. Chem. Soc.* **2007**, *129*, 8724.

[24] A. Rana, K. Bogle, O. Game, S. Patil, N. Valanoor, S. Ogale, *Appl. Phys. Lett.* **2010**, *96*, 263108.

[25] C. Chappert, A. Fert, F. N. Van Dau, *Nat. Mater.* **2007**, *6*, 813.

[26] G. W. Pabst, L. W. Martin, Y.-H. Chu, R. Ramesh, *Appl. Phys. Lett.* **2007**, *90*, 072902.

[27] H. Y. Peng, G. P. Li, J. Y. Ye, Z. P. Wei, Z. Zhang, D. D. Wang, G. Z. Xing, T. Wu, *Appl. Phys. Lett.* **2010**, *96*, 192113.

[28] a) C. Jooss, J. Hoffmann, J. Fladerer, M. Ehrhardt, T. Beetz, L. Wu, Y. Zhu, *Phys. Rev. B* **2008**, *77*, 132409; b) Y. B. Nian, J. Strozier, N. J. Wu, X. Chen, A. Ignatiev, *Phys. Rev. Lett.* **2007**, *98*, 146403; c) M. Quintero, P. Levy, A. G. Leyva, M. J. Rozenberg, *Phys. Rev. Lett.* **2007**, *98*, 116601; d) A. Sawa, T. Fujii, M. Kawasaki, Y. Tokura, *Appl. Phys. Lett.* **2004**, *85*, 4073; e) J. Son, S. Stemmer, *Phys. Rev. B* **2009**, *80*, 035105.

[29] T. Oka, N. Nagaosa, *Phys. Rev. Lett.* **2005**, *95*, 266403.

[30] S. Farokhipoor, B. Noheda, *Phys. Rev. Lett.* **2011**, *107*, 127601.

[31] H. W. Jang, D. Ortiz, S. H. Baek, C. M. Folkman, R. R. Das, P. Shafer, Y. Chen, C. T. Nelson, X. Pan, R. Ramesh, C. B. Eom, *Adv. Mater.* **2009**, *21*, 817.

[32] a) C. Kittel, *Phys. Rev.* **1946**, *70*, 965; b) T. Mitsui, J. Furuichi, *Phys. Rev.* **1953**, *90*, 193.

[33] J. Seidel, P. Maksymovych, Y. Batra, A. Katan, S. Y. Yang, Q. He, A. P. Baddorf, S. V. Kalinin, C. H. Yang, J. C. Yang, Y. H. Chu, E. K. H. Salje, H. Wormeester, M. Salmeron, R. Ramesh, *Phys. Rev. Lett.* **2010**, *105*, 197603.

[34] a) T. Choi, S. Lee, Y. J. Choi, V. Kiryukhin, S. W. Cheong, *Science* **2009**, *324*, 63; b) C. Wang, K.-j. Jin, Z.-t. Xu, L. Wang, C. Ge, H.-b. Lu, H.-z. Guo, M. He, G.-z. Yang, *Appl. Phys. Lett.* **2011**, *98*, 192901.

[35] M. J. Rozenberg, I. H. Inoue, M. J. Sanchez, *Phys. Rev. Lett.* **2004**, *92*, 178302.

[36] L. Jiang, W. S. Choi, H. Jeen, S. Dong, Y. Kim, M.-G. Han, Y. Zhu, S. V. Kalinin, E. Dagotto, T. Egami, H. N. Lee, *Nano Lett.* **2013**, *13*, 5837.